Computers and Mathematics with Applications 77 (2019) 1605–1625

Contents lists available at ScienceDirect

Computers and Mathematics with Applications

journal homepage: www.elsevier.com/locate/camwa

Accelerated numerical simulations of a heaving floating body by coupling a motion solver with a two-phase fluid solver

Brecht Devolder [a,b,*], Peter Troch [a], Pieter Rauwoens [b]

[a] Ghent University, Department of Civil Engineering, Technologiepark 904, 9052 Ghent, Belgium
[b] KU Leuven, Department of Civil Engineering, Construction Technology Cluster, Campus Bruges, Spoorwegstraat 12, 8200 Bruges, Belgium

ARTICLE INFO

Article history:
Available online 14 September 2018

Keywords:
CFD
Fluid–structure interaction
Two-phase flow
Rigid body heave motion
Accelerated coupling algorithm

ABSTRACT

This paper presents a study on the coupling between a fluid solver and a motion solver to perform fluid–structure interaction (FSI) simulations of floating bodies such as point absorber wave energy converters heaving under wave loading. The two-phase fluid solver with dynamic mesh handling, *interDyMFoam*, is a part of the Computational Fluid Dynamics (CFD) toolbox OpenFOAM. The incompressible Navier–Stokes (NS) equations are solved together with a conservation equation for the Volume of Fluid (VoF). The motion solver is computing the kinematic body motion induced by the fluid flow. A coupling algorithm is needed between the fluid solver and the motion solver to obtain a converged solution between the hydrodynamic flow field around and the kinematic motion of the body during each time step in the transient simulation. For body geometries with a significant added mass effect, simple coupling algorithms show slow convergence or even instabilities. In this paper, we identify the mechanism for the numerical instability and we derive an accelerated coupling algorithm (based on a Jacobian) to enhance the convergence speed between the fluid and motion solver. Secondly, we illustrate the coupling algorithm by presenting a free decay test of a heaving wave energy converter. Thirdly and most challenging, a water impact test of a free falling wedge with a significant added mass effect is successfully simulated. For both test cases, the numerical results obtained by using the accelerated coupling algorithm are in a very good agreement with the experimental measurements.

1. Introduction

Nowadays, floating bodies are observed everywhere in seas and oceans such as vessels, navigation buoys, berths, and floating offshore wind turbines. In particular, we focus on floating devices for marine renewable energy production. For example, wave energy converters (WECs) are used to capture wave energy from ocean waves and convert it into electrical power. In this study, WECs of the floating point absorber (FPA) type are selected of which an example is schematically visualised in Fig. 1. The WEC is moored to the seabed and heaving under wave loading. A power take-off (PTO) system is required to convert the heave motion into electricity. In order to quantify and optimise the WEC's power output, the hydrodynamic flow field around and the kinematic motion of a WEC need to be resolved. Therefore, fluid–structure interaction (FSI) simulations are performed inside a numerical wave tank (NWT) using a partitioned approach, i.e. flow and

* Corresponding author at: Ghent University, Department of Civil Engineering, Technologiepark 904, 9052 Ghent, Belgium.
E-mail addresses: Brecht.Devolder@UGent.be, Brecht.Devolder@KULeuven.be (B. Devolder), Peter.Troch@UGent.be (P. Troch), Pieter.Rauwoens@KULeuven.be (P. Rauwoens).

https://doi.org/10.1016/j.camwa.2018.08.064
0898-1221/

List of abbreviations

2D	Two Dimensional
2DV	Two Dimensional in a Vertical plane
3D	Three Dimensional
CFD	Computational Fluid Dynamics
CoM	Centre of Mass
FPA	Floating Point Absorber
FSI	Fluid–Structure Interaction
NS	Navier–Stokes
NWT	Numerical Wave Tank
PTO	Power Take-Off
RANS	Reynolds-Averaged Navier–Stokes
VoF	Volume of Fluid
WEC	Wave Energy Converter

motion equations are solved separately and a coupling algorithm is applied. The FSI simulations presented are carried out within the Computational Fluid Dynamics (CFD) toolbox OpenFOAM. CFD is able to include viscous, turbulent and non-linear effects which are absent in simplified radiation–diffraction models such as potential flow solvers based on boundary element methods [1,2]. Those effects are not only important during survivability conditions, such as extreme waves [3], but also when control strategies are applied to maximise the power output by driving the WEC's motion into resonance [4].

FSI studies have been extensively reported in the literature for a wide range of applications, see [5] and references therein. In this paper, we limit our review to a few fundamental studies and specific applications of floating bodies. An important question for FSI simulations is "How to integrate free motions of solids in fluids?". This fundamental question was studied and answered by [6]. It was reported that for bodies in a fluid of substantial density, such as water, the force acting on it strongly depends on its acceleration. This dependency originates from the inertia of the water particles surrounding the body, which are also accelerated when the body accelerates, as their motion is determined by the motion of the body through the boundary condition on the wetted surface of that body. The mass of the surrounding fluid (i.e. water) moving along with an accelerating or decelerating body is also called the added mass. For a floating body installed in a sea or ocean, the added mass is not only depending on the geometry but also on the incoming wave conditions [7]. Due to added mass effects, explicit fluid–motion coupling (also known as loosely or weakly coupled techniques) is only conditionally stable. The stability is significantly enhanced by using implicit (or strongly coupled) techniques but multiple sub iterations are needed during every time step to obtain convergence between the fluid and motion solver, increasing the computational time significantly [8]. [9] performed simulations of a rigid body moving in one degree of freedom in an incompressible fluid (single phase) with a density significantly larger than the density of the body. They demonstrated that both a standard explicit coupling scheme and an implicit procedure with explicit coupling in the sub iterations show stability issues. They suggested a procedure with implicit coupling in the sub iterations by using numerically computed derivatives (i.e. a Jacobian). For some applications, the assumption of a rigid body is not valid (e.g. inflatable storm surge barriers) and deformation of the fluid–structure interface is calculated by a structural solver. [5] presented a complete overview on partitioned simulation techniques using two black-box solvers (fluid and structural solver) for strongly coupled FSI problems. Different partitioned simulation techniques were formulated, reviewed and compared to each other in terms of implementation and performance (e.g. number of sub iterations during every time step). They reported that the Gauss–Seidel iteration scheme was accelerated

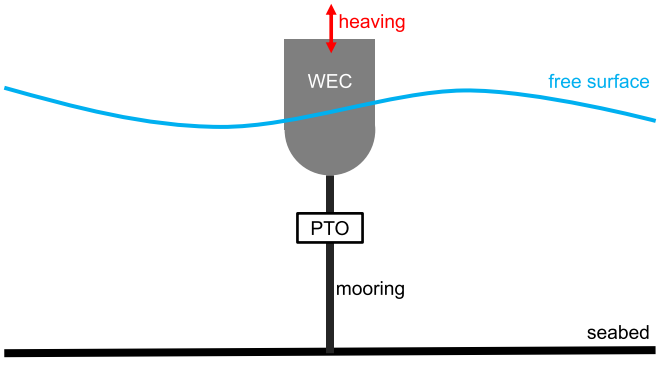

Fig. 1. Definition sketch of a floating point absorber wave energy converter. The motion of the WEC is restricted to heave only. The WEC is moored to the seabed and a power take-off (PTO) system is required for electricity production.

by using dynamic Aitken's relaxation [10]. Even larger accelerations were found by using more advanced state-of-the-art coupling algorithms such as IQN-ILS and IBQN-LS. More recently, [11–14] presented FSI simulations using a coupled two-phase fluid solver with a rigid body motion solver. [11] developed a strongly coupled model using sub iterations and dynamic Aitken's relaxation to take the added mass effect into account. They also reported a verification and validation study of a two dimensional (2D) heaving cylinder indicating promising results. In addition, [12] showed a reduction in simulation times varying between 70% and 80% for using Aitken's relaxation compared to fixed relaxation. They also observed that Aitken's relaxation converged much faster during the first 10–20 sub iterations compared to fixed relaxation. Their motion solver was based on a second order Adams–Bashforth–Moulton explicit–implicit scheme. [13] studied the water impact and entry of a free falling wedge using the CFD toolbox REEF3D. They found a good agreement between numerical and experimental results for the vertical position and velocity of the wedge. The motion of the wedge was represented by the level set method in order to avoid mesh motion or overset meshes. [14] implemented a fifth-order Cash–Karp embedded Runge–Kutta scheme with error control and adaptive time-step size. The motion solver was called after every solution of the pressure equation in order to enhance the convergence of the coupled fluid–motion solver. In every sub iteration, the change of the body's velocity was directly incorporated in the pressure equation by means of a source term but the mesh was only moved once per time step. Their method resulted in an acceleration of a factor two and more for the CPU time to perform seakeeping simulations of a container ship.

For the application of floating bodies, two facts must be considered. Firstly, water impact tests and wave-induced body motions cause a temporal variation of the added mass. Secondly, if the added mass is larger than the physical mass, the fluid–motion coupling features stability issues. Based on a review of those previous studies, different algorithms exist to stabilise partitioned FSI simulations. Most of them are derived for coupling two black-box solvers which are inaccessible, i.e. a fluid solver and a structural solver. In our case of a rigid body, the structural solver is simplified to a motion solver which is merely an integration of Newton's second law. In this manuscript, we show that a stability issue in the coupling between the fluid solver and the motion solver can be resolved on the condition that a good estimate for the added mass is obtained, as suggested in [6]. We compute the added mass using an accelerated coupling algorithm based on [9], i.e. implicit coupling in the sub iterations by calculating a Jacobian.

This paper presents a study on the coupling between a fluid solver and a motion solver for simulating a floating body in a NWT. We are using the two-phase fluid solver with dynamic mesh handling, *interDyMFoam*, which is a part of the CFD toolbox OpenFOAM. Only the dominant motion of a WEC is considered, the heave motion, which allows a reduction from a six to a one degree of freedom motion. We derive an accelerated coupling algorithm for cases with a significant added mass effect to stabilise the fluid–motion coupling. Both stabilisation and acceleration are achieved by applying implicit coupling in the sub iterations and by calculating a Jacobian. The performance of the coupled fluid–motion solver is validated by using two test cases involving floating bodies: a free decay test of a WEC and a water impact test of a free falling wedge with a significant added mass effect.

The remainder of this paper is organised as follows. Firstly in Section 2, the governing equations for both the fluid and motion solver are presented. In Section 3, the accelerated coupling algorithm between a fluid and motion solver is derived. Subsequently in Section 4, the coupled fluid–motion solver is applied to perform FSI simulations of a free decay test of a heaving WEC and a water impact test of a free falling wedge. Finally, the conclusions are drawn in Section 5.

2. Numerical model

In this section, the numerical methods used to study FSI problems in OpenFOAM® [15], version 3.0.1 are summarised. Both, the governing equations for the fluid and motion solver are formulated, respectively, followed by the kinematic condition at the fluid–structure interface.

2.1. Fluid solver

The two-phase fluid solver uses the three dimensional (3D) incompressible Reynolds-Averaged Navier–Stokes (RANS) equations to express the motion of the two fluids (i.e. water and air). The RANS equations consist of a mass conservation Eq. (1) and a momentum conservation Eq. (2) written in Einstein summation notation as follows:

$$\frac{\partial u_i}{\partial x_i} = 0 \tag{1}$$

$$\frac{\partial \rho u_i}{\partial t} + \frac{\partial \rho u_j u_i}{\partial x_j} - \frac{\partial}{\partial x_j}\left[\mu_{eff}\frac{\partial u_i}{\partial x_j}\right] = -\frac{\partial p^*}{\partial x_i} + F_{b,i} + f_{\sigma,i} \tag{2}$$

in which t is the time, u_i $(i = x, y, z)$ are the Cartesian components of the fluid velocity, ρ is the fluid density, μ_{eff} is the effective dynamic viscosity, p^* is the pressure in excess of the hydrostatic, F_b is an external body force (including gravity) which is defined as follows:

$$F_{b,i} = -g_i x_i \frac{\partial \rho}{\partial x_i} \tag{3}$$

Table 1
Default values for ϕ_1 and ϕ_2 used in Eq. (10) to calculate σ_k, σ_ω, β and γ for the k-ω SST model.

ϕ	σ_k	σ_ω	β	γ
ϕ_1	0.85034	0.5	0.075	0.5532
ϕ_2	1.0	0.85616	0.0828	0.4403

in which the gravitational acceleration vector $\vec{\boldsymbol{g}} = [0; 0; -9.81]\,\mathrm{m/s^2}$ and $\vec{\boldsymbol{x}}$ is the Cartesian coordinate vector (x, y, z). f_σ is the surface tension tensor term which is neglected in the present study. Note that the mean values for the variables considered are written in terms of Favre-averaging (density weighted) due to the varying density in the NWT.

The interface between water and air is obtained by the Volume of Fluid (VoF) method using a compression term as documented in [16]. The method is based on a volume fraction α which is 0 for a completely dry cell and 1 for a completely wet cell and in between 0 and 1 for an interface cell containing both water and air. The volume fraction is solved by an advection Eq. (4):

$$\frac{\partial \alpha}{\partial t} + \frac{\partial u_i \alpha}{\partial x_i} + \frac{\partial u_{c,i} \alpha\,(1-\alpha)}{\partial x_i} = 0 \tag{4}$$

The last term on the left-hand side is an artificial compression term where $u_{c,i} = \min[c_\alpha |u_i|, \max(|u_i|)]$. In the present study, the default value of c_α equal to 1 is applied.

The density of the fluid ρ within a computational cell is calculated by a weighted value based on the volume fraction α. The effective dynamic viscosity μ_{eff} is obtained by the sum of a weighted value based on the volume faction α and an additional turbulent dynamic viscosity $\rho \nu_t$:

$$\rho = \alpha \rho_{water} + (1-\alpha)\,\rho_{air} \tag{5}$$

$$\mu_{eff} = \alpha \mu_{water} + (1-\alpha)\,\mu_{air} + \rho \nu_t \tag{6}$$

If a laminar solution is sufficiently accurate, the turbulent kinematic viscosity ν_t is equal to zero. In the other case, turbulent effects are incorporated in the RANS Eqs. (1) and (2) by solving one or more additional transport equations to yield a value for the turbulent kinematic viscosity ν_t. In the present study, a buoyancy-modified $k-\omega$ *SST* model is applied which has been developed in previous works of the authors [17,18]. A buoyancy-modified turbulence model not only results in a stable wave propagation model without wave damping [17] but it also predicts the turbulence level inside the flow field more accurately in the surf zone where waves break [18]. The buoyancy-modified $k-\omega$ *SST* model is defined as follows:

$$\frac{\partial \rho k}{\partial t} + \frac{\partial \rho u_j k}{\partial x_j} - \frac{\partial}{\partial x_j}\left[\rho\,(\nu + \sigma_k \nu_t)\,\frac{\partial k}{\partial x_j}\right] = \rho P_k + G_b - \rho \beta^* \omega k \tag{7}$$

$$\frac{\partial \rho \omega}{\partial t} + \frac{\partial \rho u_j \omega}{\partial x_j} - \frac{\partial}{\partial x_j}\left[\rho\,(\nu + \sigma_\omega \nu_t)\,\frac{\partial \omega}{\partial x_j}\right] = \frac{\gamma}{\nu_t}\rho G - \rho \beta \omega^2 + 2\,(1-F_1)\,\rho \frac{\sigma_{\omega 2}}{\omega}\frac{\partial k}{\partial x_j}\frac{\partial \omega}{\partial x_j} \tag{8}$$

$$P_k = \min(G, 10\beta^* k\omega) \qquad G = \nu_t \frac{\partial u_i}{\partial x_j}\left(\frac{\partial u_i}{\partial x_j} + \frac{\partial u_j}{\partial x_i}\right) \qquad \nu_t = \frac{a_1 k}{\max(a_1 \omega, SF_2)} \tag{9}$$

where k is the turbulent kinetic energy, P_k is the production term of k, ν is the kinematic viscosity, ν_t is the turbulent kinematic viscosity, ω is the specific dissipation rate, S is the mean rate of strain of the flow, $\beta^* = 0.09$ and $a_1 = 0.31$. F_1 and F_2 are blending functions. F_1 is designed to be one in the near wall region (activating $k-\omega$) and zero away from the wall (activating $k-\varepsilon$) [19]. The values of σ_k, σ_ω, β and γ are blended using Eq. (10) in which ϕ_1 and ϕ_2 are given in Table 1.

$$\phi = F_1 \phi_1 + (1-F_1)\,\phi_2 \tag{10}$$

The buoyancy term G_b is treated implicitly and the scalar $\sigma_t = 0.85$ [17]:

$$G_b = -\frac{\nu_t}{\sigma_t}\frac{\partial \rho}{\partial x_j} g_j \tag{11}$$

2.2. Motion solver

In this study, the motion solver is restricted to one degree of freedom, only the heave motion is allowed (Z-direction). The motion solver calculates the vertical position of the body by applying Newton's second law at the current time $n+1$:

$$F^{n+1} = m a^{n+1} \tag{12}$$

in which F^{n+1} is the overall vertical force (including gravity) obtained with the fluid solver by integrating the pressure and shear forces acting the body's surface and a^{n+1} is the vertical acceleration of the body. Once the acceleration a^{n+1} is known, the vertical velocity v^{n+1} and the vertical position z^{n+1} during the same time $n+1$ are calculated by an integration scheme:

$$v^{n+1} = v^n + (1-\theta)a^n \Delta T + \theta a^{n+1} \Delta T \tag{13}$$

$$z^{n+1} = z^n + (1-\theta)v^n \Delta T + \theta v^{n+1} \Delta T \tag{14}$$

in which n is the previous time, $n+1$ is the current time, ΔT is the time step and θ is a blending parameter. For $\theta = 0$, the forward Euler method arises which is explicit in time. In case $\theta = 1$, the backward Euler method pops up which is fully implicit in time. Both methods are only first order accurate leading to additional numerical damping. In order to improve the accuracy of the body's motion, a second order accurate Crank–Nicolson scheme is applied for the FSI studies presented by using $\theta = 0.5$. An additional asset of the Crank–Nicolson scheme is that it preserves the total amount of energy, i.e. the sum of kinetic and potential energy.

The new position of the body z^{n+1} serves as a boundary condition for the mesh motion operation which is organised that only the highest and lowest row of cells is distorted (compressed or expanded). An example is demonstrated in Figs. 8 and 18 later in this paper. This methodology is implemented to prevent undesirable mesh deformation (i.e. high non-orthogonality and skewness of the grid cells) around the air–water interface, reducing the discretisation error for the applied finite volume method. This also results in accurate simulations of a floating body using the coupled fluid–motion solver based on the VoF method. The drawback of our approach is that high aspect ratios are obtained for the distorted cells. However since those cells are not inside the zones of interest, it will not affect the accuracy of the simulations.

2.3. Kinematic condition

In order to have convergence between the fluid and motion solver, the following kinematic condition needs to be fulfilled at the interface between the fluid and the body:

$$u_z = v \tag{15}$$

in which u_z and v are the vertical fluid velocity and the vertical body's velocity, respectively. As such, this velocity is used in the moving wall boundary condition at the body's interface. Note that the fluid velocities u_x and u_y are equal to 0 m/s at the fluid–structure interface because only heave motion of the body is allowed.

3. Accelerated coupling algorithm

This section presents the accelerated coupling algorithm between a two-phase fluid solver (Section 2.1) and a one degree of freedom (heave) motion solver (Section 2.2). For the sake of clarity, the complexity of the fluid solver is gradually increased. Firstly, the motion solver is tested against a mock-up fluid solver which is an analytical expression describing the fluid dynamics. Secondly, an acceleration in convergence between the CFD fluid solver and the motion solver is developed to speed up the simulations in terms of CPU time.

3.1. Mock-up fluid solver

The coupling between a fluid and a motion solver in rigid body simulations is done by interchanging the total force acting on the body calculated by the fluid solver. For a CFD fluid solver, the force (vector notation) is calculated as the discrete sum of the pressure forces, viscous forces and the downward weight of the body:

$$\vec{\mathbf{F}}^{\mathbf{n+1}} = \sum_{j}^{body} \left(p_j \vec{\boldsymbol{n}}_{\boldsymbol{j}} A_j\right) + \sum_{j}^{body} \left(\vec{\vec{\boldsymbol{\tau}}}_{\boldsymbol{j}} \vec{\boldsymbol{n}}_{\boldsymbol{j}} A_j\right) - m\vec{\boldsymbol{g}} \tag{16}$$

p_j is the pressure acting on each boundary face around the body, $\vec{\vec{\boldsymbol{\tau}}}_{\boldsymbol{j}}$ is the shear stress tensor acting on each boundary face around the body, $\vec{\boldsymbol{n}}_{\boldsymbol{j}}$ is a unit vector normal to the area A_j of boundary face j and m is the dry mass of the body.

In this subsection, the CFD fluid solver is simplified to a mock-up fluid solver: an analytical expression which calculates the total vertical force F^{n+1} on the body. The main advantage of the mock-up fluid solver is to avoid the time consuming CFD fluid solver when acquiring quick insights in the coupling algorithm. The floating body is represented by a two dimensional rectangular body in a vertical plane (2DV) which is 4 m wide, 1 m high and has a mass m equal to 2000 kg/m (see Fig. 2). z^{eq} is the fixed Z-coordinate of the equilibrium position of the body's Centre of Mass (CoM). In order to bring the body out of equilibrium, the position of the CoM during the initial condition is $z^n < z^{eq}$, see Fig. 2. As a result, the water exerts an upward force on the body and the body starts to oscillate until all the forces on the body are again in equilibrium.

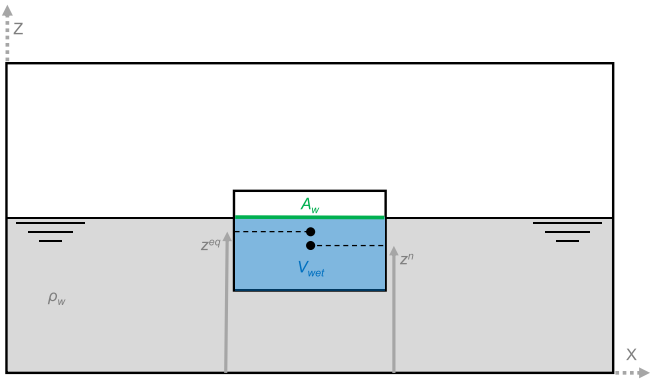

Fig. 2. A definition sketch showing the geometry of the floating 2D rectangular body (XZ-direction, 4 m wide by 1 m high) with mass m equal to 2000 kg/m.

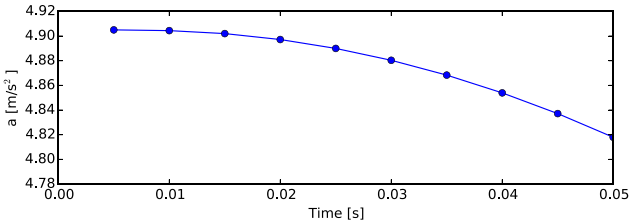

Fig. 3. Vertical acceleration of the floating 2D rectangular body as a function of time for a fixed time step of 0.005 s.

3.1.1. Hydrostatic force

The initial mock-up fluid solver takes only the upward hydrostatic force and the body's weight into account. The total vertical force on the 2D rectangular body is calculated as follows:

$$\begin{aligned} F^{n+1} &= \rho_w V_{wet} g - \\ mg &= -\rho_w A_{wet} g \left(z^n - z^{eq}\right) \end{aligned} \tag{17}$$

in which ρ_w is the density of water (1000 kg/m^3), V_{wet} is the underwater volume of the body, A_{wet} is the horizontal water plane area and $z^n - z^{eq}$ is the distance between the *CoM* at the previous time n and the *CoM* in equilibrium (see Fig. 2). Note that Eq. (17) is explicit: we use the body's position from the previous time, z^n, to calculate the force during the current time, F^{n+1}. Newton's second law, Eq. (12), is applied to derive the body's acceleration during the current time $n+1$ by using the mock-up fluid solver (Eq. (17)):

$$\begin{aligned} a^{n+1} &= \frac{F^{n+1}}{m} \\ &= \frac{-\rho_w A_{wet} g}{m} \left(z^n - z^{eq}\right) \\ &= -\frac{k}{m} \left(z^n - z^{eq}\right) \end{aligned} \tag{18}$$

in which k is the restoring spring coefficient due to buoyancy and equal to 39 240 kg/s^2 for the 2D rectangular body. The mock-up fluid solver (Eq. (18)) is coupled to the motion solver (Eqs. (13) and (14) with $\theta = 0.5$ and a fixed time step $\Delta T = 0.005$ s). An initial displacement of -0.25 m is given to the body in order to bring it out of equilibrium ($z^0 = 4.75$ m and $z^{eq} = 5.0$ m). Eqs. (18), (13) and (14) are solved consecutively and only once during every time step due to the explicit nature of the fluid–motion coupling. The resulting vertical acceleration, Eq. (18), as a function of time is shown in Fig. 3. The progress of the acceleration matches the expectations, starting at a maximum value and reducing monotonically without any issues regarding stability or convergence.

3.1.2. Added mass effect

In a second step, the added mass effect is also considered in the explicit mock-up fluid solver:

$$ma^{n+1} = -m_a a^n - k\left(z^n - z^{eq}\right) \tag{19}$$

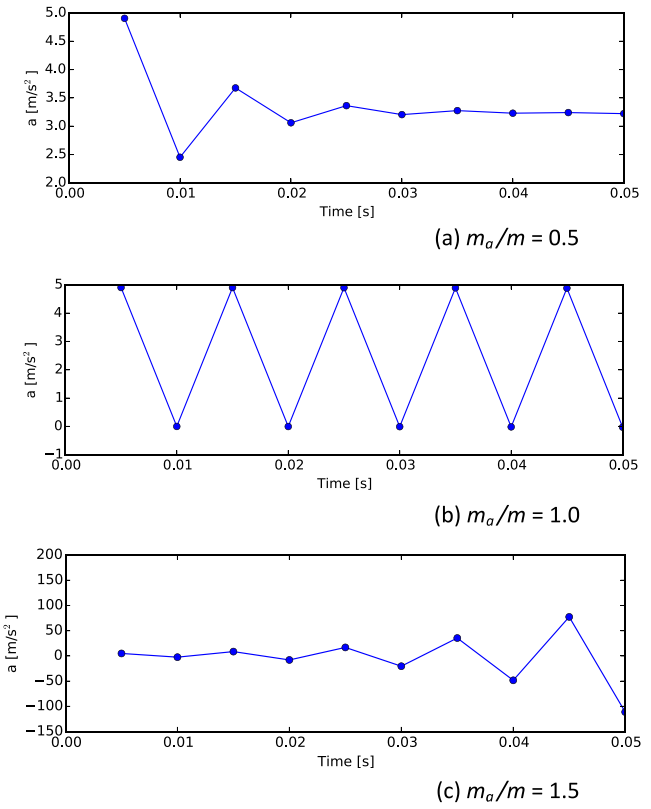

Fig. 4. Vertical acceleration of the floating 2D rectangular body as a function of time for $m_a/m = 0.5$ (a), 1.0 (b) and 1.5 (c).

in which m_a is the added mass and a^n is the acceleration at the previous time n. This is a better approximation to the physics because all the fluid dynamics are incorporated, except for the viscous forces (damping forces). Subsequently, Eq. (19) is rewritten to

$$a^{n+1} = -\frac{m_a}{m}a^n - \frac{k}{m}\left(z^n - z^{eq}\right) \tag{20}$$

The extended mock-up fluid solver (Eq. (20)) is again coupled to the motion solver (Eqs. (13) and (14) with $\theta = 0.5$ and a fixed time step $\Delta T = 0.005$ s) and solved once during every time step. Three different numerical simulations are performed with $m_a/m = 0.5$, 1.0 and 1.5. Fig. 4 shows the numerical results for the acceleration, Eq. (20), as a function of time. In case $m_a < m$, the oscillation in acceleration damps out. For $m_a = m$, the oscillation remains constant. For $m_a > m$, the oscillation increases and the simulation fails.

To stabilise the acceleration, Eq. (20) must be solved implicitly by using multiple sub iterations during every time step:

$$\tilde{a}_{i+1}^{n+1} = -\frac{m_a}{m}a_i^{n+1} - \frac{k}{m}\left(z_i^{n+1} - z^{eq}\right) \tag{21}$$

in which $\tilde{a}_{i+1}^{n+1}$ is the intermediate value of the acceleration at the current sub iteration $i+1$ of time $n+1$, a_i^{n+1} and z_i^{n+1} are, respectively, the acceleration and position of the *CoM* from the previous sub iteration i during the same time $n+1$. Note that Eq. (21) is using explicit coupling in the sub iterations: all the variables in the right hand side are obtained during the previous sub iteration i. Additionally, relaxation of acceleration is required for a stable solution:

$$a_{i+1}^{n+1} = \alpha\tilde{a}_{i+1}^{n+1} + (1-\alpha)a_i^{n+1} \tag{22}$$

in which α is the relaxation factor. In order to know the stability region of the coupling scheme, a linear stability analysis is performed for Eqs. (21) and (22):

$$\begin{aligned} a_{i+1}^{n+1} &= \alpha\tilde{a}_{i+1}^{n+1} + (1-\alpha)a_i^{n+1} \\ &= -\alpha\frac{k}{m}\left(z_i^{n+1} - z^{eq}\right) - \alpha\frac{m_a}{m}a_i^{n+1} + (1-\alpha)\,a_i^{n+1} \end{aligned}$$

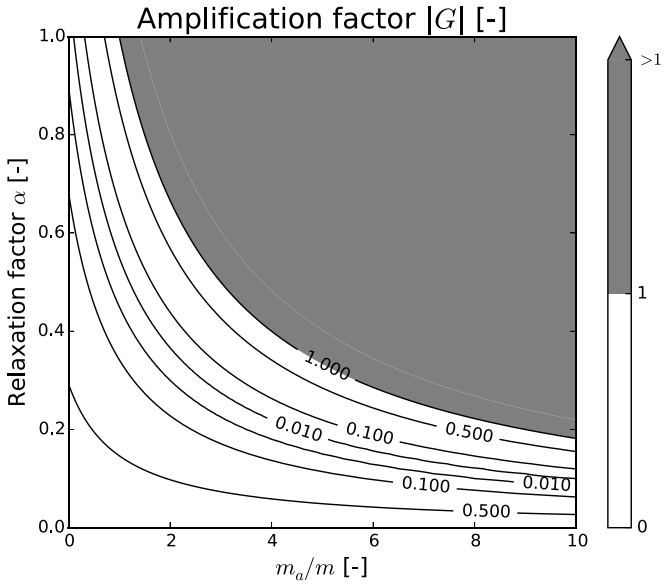

Fig. 5. Contour plot of the amplification factor $|G|$ for Eqs. (21) and (22) as a function of the added mass coefficient m_a/m and the relaxation factor α. The grey shaded area is unstable whereas the decreasing values of the amplification factor are leading to faster simulation times.

$$\begin{aligned} &= -\alpha \frac{k}{m} \left(z_i^{n+1} - z^{eq}\right) + \left(1 - \alpha - \alpha \frac{m_a}{m}\right) a_i^{n+1} \\ &= -\alpha \frac{k}{m} \left(z_i^{n+1} - z^{eq}\right) + G a_i^{n+1} \end{aligned} \tag{23}$$

in which G is defined as the amplification factor. In order to have a stable solution, the absolute value of G must be smaller than one:

$$\begin{aligned} |G| &\leq 1 \\ G^2 &\leq 1 \\ \left(1 - \alpha - \alpha \frac{m_a}{m}\right)^2 &\leq 1 \end{aligned} \tag{24}$$

which results in a stability criterion for α and an optimal value, $\alpha_{optimal}$, for which G is equal to 0:

$$\alpha \leq \frac{2}{1 + m_a/m} \tag{25}$$

$$\alpha_{optimal} = \frac{1}{1 + m_a/m} = \frac{m}{m + m_a} \tag{26}$$

The stability region $|G| \leq 1$ as a function of the added mass coefficient m_a/m and α is depicted in Fig. 5 as an unshaded area whereas the unstable region is shaded in grey. The contour lines indicate the value of the amplification factor $|G|$. The closer the relaxation factor is to its optimal value, the closer the amplification factor to zero and the lesser sub iterations are needed between the fluid and motion solver to converge. More importantly, a low number of sub iterations speeds up the simulation significantly in terms of CPU time.

The mock-up fluid solver (Eq. (22) with $m_a = 3m$) is coupled to the motion solver (Eqs. (13) and (14) with $\theta = 0.5$ and a fixed time step $\Delta T = 0.005$ s) and now 20 sub iterations per time step are performed. Fig. 6 depicts the acceleration, Eq. (22), as a function of the number of sub iterations. In Fig. 6, the red line represents the coupling scheme using a relaxation factor equal to 0.25, which is exact $\alpha_{optimal} = m/(m + m_a)$ (Eq. (26)). Only one iteration is needed to reach convergence in the acceleration. In case the relaxation factor is 0.45 (green line in Fig. 6), convergence is reached with oscillations. With a relaxation factor of 0.05 (blue line in Fig. 6), convergence is reached monotonically. The converged value of the acceleration during every time step is the same for the three different relaxation factors but the convergence speed is different. In order to obtain efficient simulations with a minimal number of sub iterations for cases with a significant added mass effect ($m_a > m$), the relaxation factor must not deviate too much from its optimal value (see Eq. (26)).

3.2. CFD fluid solver

In Section 3.1, we have demonstrated a significant acceleration in convergence between a mock-up fluid solver and a motion solver. In case the value of the added mass is known, the optimal value for the relaxation factor is calculated by

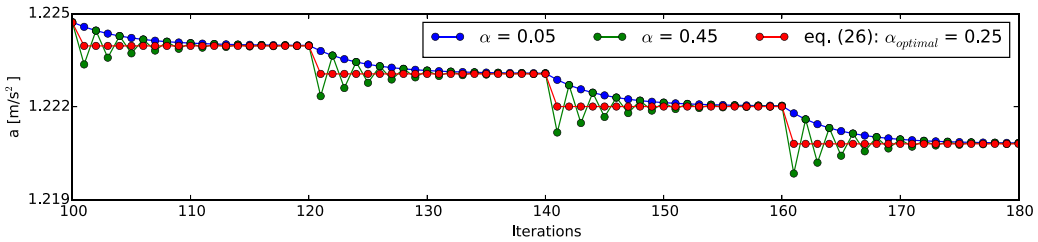

Fig. 6. Vertical acceleration of the floating 2D rectangular body as a function of the number of sub iterations for different values of α and Eq. (26). During each time step, 20 iterations are performed ($m_a/m = 3.0$). (For interpretation of the references to colour in this figure legend, the reader is referred to the web version of this article.)

Eq. (26). In this section, we go one step further from the mock-up fluid solver to a CFD fluid solver where the value of the added mass is unknown.

3.2.1. Estimation of the added mass

In order to achieve an acceleration in convergence between a CFD fluid solver and a motion solver, we apply the method reported in [9]: calculating a Jacobian. Therefore, Newton's second law in its fully implicit state, Eq. (27), is linearised to Eq. (28), resulting in Eq. (29).

$$F_{i+1}^{n+1} = ma_{i+1}^{n+1} \tag{27}$$

$$F_i^{n+1} + \left(\frac{\mathrm{d}F}{\mathrm{d}a}\right)_i^{n+1} \left(a_{i+1}^{n+1} - a_i^{n+1}\right) \approx ma_{i+1}^{n+1} \tag{28}$$

$$a_{i+1}^{n+1} \approx \frac{F_i^{n+1} - \left(\frac{\mathrm{d}F}{\mathrm{d}a}\right)_i^{n+1} a_i^{n+1}}{m - \left(\frac{\mathrm{d}F}{\mathrm{d}a}\right)_i^{n+1}} \tag{29}$$

Note that Eq. (27) is using implicit coupling in the sub iterations: the variables on both left and right hand side are considered on the same sub iteration $i+1$. The total derivative $\left(\frac{\mathrm{d}F}{\mathrm{d}a}\right)_i^{n+1}$ is estimated by the difference quotient:

$$\left(\frac{\mathrm{d}F}{\mathrm{d}a}\right)_i^{n+1} \approx \frac{F_i^{n+1} - F_1^{n+1}}{a_i^{n+1} - a_1^{n+1}} \tag{30}$$

In order to know the physical meaning of $\left(\frac{\mathrm{d}F}{\mathrm{d}a}\right)_i^{n+1}$, a mass–spring–damper system is assumed and the total force F_i^{n+1} is decomposed in an added mass force, a hydrodynamic damping force, a hydrostatic restoring force (i.e. buoyancy) and the sum of all other external forces:

$$F_i^{n+1} = -m_a a_i^{n+1} - bv_i^{n+1} - k(z_i^{n+1} - z^{eq}) + \sum_k F_{ext,k} \tag{31}$$

in which m_a is the added mass, b is the hydrodynamic damping coefficient and k is the restoring spring coefficient (see also Section 3.1.1). z^{eq} is a fixed value representing the equilibrium position of floating body. $F_{ext,k}$ is an external force independent of the kinematic motion of the body, such as the exiting wave force or a PTO force for the case of WECs. By substituting Eqs. (13) and (14) with $\theta = 0.5$ in Eq. (31), $\left(\frac{\mathrm{d}F}{\mathrm{d}a}\right)_i^{n+1}$ is equal to:

$$\begin{aligned}\left(\frac{\mathrm{d}F}{\mathrm{d}a}\right)_i^{n+1} &= \left(\frac{\partial F}{\partial a}\right)_i^{n+1}\frac{\mathrm{d}a}{\mathrm{d}a} + \left(\frac{\partial F}{\partial v}\right)_i^{n+1}\frac{\mathrm{d}v}{\mathrm{d}a} + \left(\frac{\partial F}{\partial z}\right)_i^{n+1}\frac{\mathrm{d}z}{\mathrm{d}a} \\ &= -m_a - b\frac{\mathrm{d}v}{\mathrm{d}a} - k\frac{\mathrm{d}z}{\mathrm{d}a} \\ &= -m_a - \frac{1}{2}b\Delta T - \frac{1}{4}k(\Delta T)^2\end{aligned} \tag{32}$$

[6] reported that a significant part of the force depends on the acceleration for fluids of substantial density such as water. If this assumption is valid, m_a is the dominating component and $b\frac{\mathrm{d}v}{\mathrm{d}a}$ or $\frac{1}{2}b\Delta T$ and $k\frac{\mathrm{d}z}{\mathrm{d}a}$ or $\frac{1}{4}k(\Delta T)^2$ are small values in Eq. (32). The assumption is checked later in this paper for the applications presented (see Section 4). Consequently, $\left(\frac{\mathrm{d}F}{\mathrm{d}a}\right)_i^{n+1}$ is approximated by

$$\left(\frac{\mathrm{d}F}{\mathrm{d}a}\right)_i^{n+1} \approx -m_a \tag{33}$$

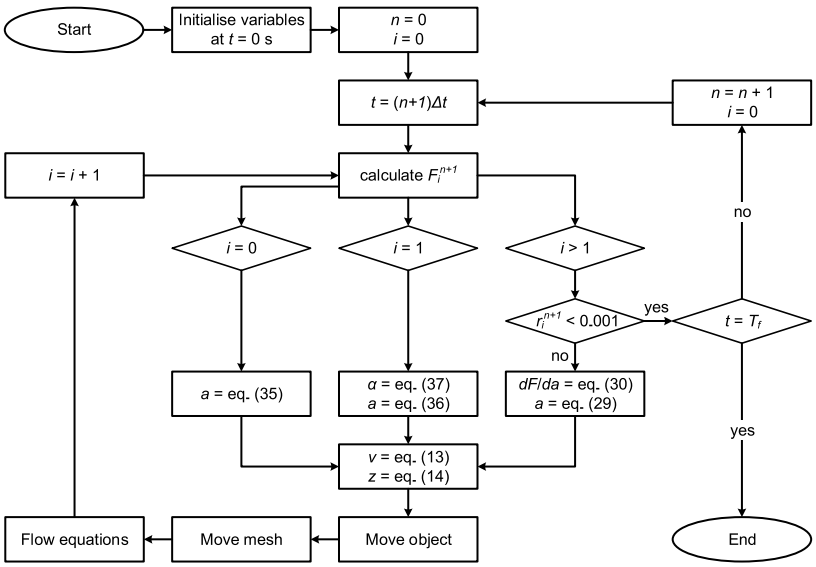

Fig. 7. Flowchart of the coupled fluid–motion solver using an accelerated coupling algorithm. n is the time and i indicates the sub iteration.

This demonstrates a strong relation between $\left(\frac{\mathrm{d}F}{\mathrm{d}a}\right)_i^{n+1}$ and the added mass m_a:

$$m_a \approx -\left(\frac{\mathrm{d}F}{\mathrm{d}a}\right)_i^{n+1} \approx -\frac{F_i^{n+1} - F_1^{n+1}}{a_i^{n+1} - a_1^{n+1}} \tag{34}$$

In order to estimate the added mass by calculating a Jacobian, we need at least three sub iterations during every time step:

- a_1^{n+1}: the acceleration during the first sub iteration ($i = 0$);
- F_1^{n+1}: the force resulting from the hydrodynamic flow field during the first sub iteration ($i = 0$);
- F_i^{n+1}: the force resulting from the hydrodynamic flow field during the second or higher sub iteration ($i > 1$). Note that due to the numerical implementation, the force F_i^{n+1} is only called in sub iteration $i+1$ by the motion solver (see the flowchart in Fig. 7 later in this paper).

3.2.2. Numerical implementation

The numerical implementation of the accelerated coupling algorithm is shown in Fig. 7. At the start of a FSI simulation, all the variables are initialised, such as the pressure and velocity. For each time step, there are $i+1$ sub iterations needed to reach convergence between the fluid and motion solver. Acceleration in convergence is obtained by computing $\left(\frac{\mathrm{d}F}{\mathrm{d}a}\right)_i^{n+1}$ to estimate the added mass m_a for which we need at least three sub iterations (see Section 3.2.1):

1. During the first sub iteration ($i = 0$), the body's position is calculated based on the final acceleration during the previous time step a^n increased with a small constant value δ [9]:

$$a_{i+1}^{n+1} = a^n + \delta \tag{35}$$

The value of δ is a few orders of magnitude lower (2 or 3) than the maximum acceleration and is therefore application dependent and user defined. As reported by [9], the hydrodynamic flow field and the kinematic motion during every time step are not sensitive to the value of δ.

2. In the second sub iteration ($i = 1$), relaxation of acceleration is performed:

$$\begin{aligned} a_{i+1}^{n+1} &= \alpha^n \tilde{a}_{i+1}^{n+1} + (1-\alpha^n) a_i^{n+1} \\ &= \alpha^n \frac{F_i^{n+1}}{m} + (1-\alpha^n) a_i^{n+1} \end{aligned} \tag{36}$$

in which a_i^{n+1} is the acceleration from the first sub iteration and is equal to $a^n + \delta$. During the first time step, the relaxation factor α^n is user defined. In all the other time steps, the relaxation factor is updated based on the estimated

value of m_a (Eq. (34)) during the previous time step:

$$\alpha^n = \frac{m}{m + (m_a)^n} \approx \frac{m}{m - \left(\frac{dF}{da}\right)^n} \tag{37}$$

By following this methodology during the 2nd sub iteration, we only need two sub iterations to have a convergence between the fluid and motion solver for two scenario's: (i) if the added mass is significantly smaller than the mass or (ii) if the added mass is not varying significantly between two consecutive time steps.

3. In all the following sub iterations ($i > 1$), $\left(\frac{dF}{da}\right)_i^{n+1}$ and a_{i+1}^{n+1} are calculated by Eqs. (29) and (30), respectively. To avoid overshoots in the coupling algorithm, the estimated value of the added mass is bounded between 0 and $10m$. This assumption is valid since the added mass of a floating body cannot be negative nor exceed the value of $10m$ for practical applications in unrestricted water.

Once the acceleration is calculated in a specific sub iteration, the vertical velocity and position of the body are computed by Eqs. (13) and (14), respectively. Subsequently, the body is moved, the mesh motion is performed and the flow Eqs. (1), (2), (4), (7) and (8) are solved to obtain the hydrodynamics flow field. This iterative procedure stops until convergence between the fluid and motion solver (i.e. Newton's second law, Eq. (27)) is achieved within a certain time step. During every sub iteration ($i > 1$), the normalised residual r_i^{n+1} is calculated as follows:

$$r_i^{n+1} = \frac{\left|F_i^{n+1} - ma_i^{n+1}\right|}{F_{\max}} \tag{38}$$

in which $F_{\max}$ is a representative value for the maximum force during a simulation. The convergence criterion is formulated such that the normalised residual must be lower than a threshold, 0.001 for example [9,12].

4. Applications

In this section two test cases are presented using the accelerated coupling algorithm for the fluid–motion solver elaborated in Section 3.2. For all simulations the following settings are used in the fluid solver: second order linear discretisation for the gradient and the Laplacian; first/second order bounded Van Leer scheme for the divergence operators; second order, bounded, implicit time discretisation. For every time step, maximum 50 sub iterations are performed depending on the residual calculated with Eq. (38).

4.1. Free decay test of a WEC

For the first application, a 3D WEC is modelled and a free decay test is performed. Numerical results are compared with experimental data which are described in previous work of the authors [20]. The same numerical method is used as reported in [20] but instead of applying a fixed relation factor for the acceleration, the accelerated coupling algorithm is used. In this study, a maximum Courant number of 0.3 and a vertical grid size Δz equal to 0.02 m are used (see verification study in [20] for a fixed time step).

4.1.1. Computational domain

The numerical wave flume is represented by a structured grid consisting of only hexahedral cells (139 058 cells). An overview of the numerical domain around the WEC during a free decay test is depicted in Fig. 8. In panels (a) and (b), the initial condition is shown, where blue is water, red is air and green represents 50% water and 50% air. In panel (c), the maximum displacement of the mesh points during the numerical simulation is visualised ($t = 0.55$ s).

4.1.2. Boundary conditions

Two symmetry planes are used to reduce the amount of grid cells, see [20]. The bottom and side walls of the numerical wave flume are modelled as a solid wall: a Dirichlet boundary condition is set for the velocity (0 m/s in the two directions) while the pressure and volume fraction are set to a Neumann condition. At the outlet, wave absorption is implemented using the IHFOAM toolbox [21,22]. On all the boundary faces of the WEC, the velocity vector is set to a moving wall condition (see Eq. (15)) and the pressure and volume fraction are set to a Neumann condition. The atmospheric conditions at the top of the numerical domain are set to a mixed Dirichlet–Neumann boundary condition for the velocity, pressure and volume fraction. Finally, the value for δ in Eq. (35) is equal to 1.0 m/s^2.

Turbulent effects are not expected since no water impact events will happen nor separation of the flow behind the WEC will occur (low Keulegan–Carpenter number). Therefore in the first instance, only laminar solutions are generated. As shown later on, the main features of the WEC's motion and radiated wave field are already captured by using a laminar solution only.

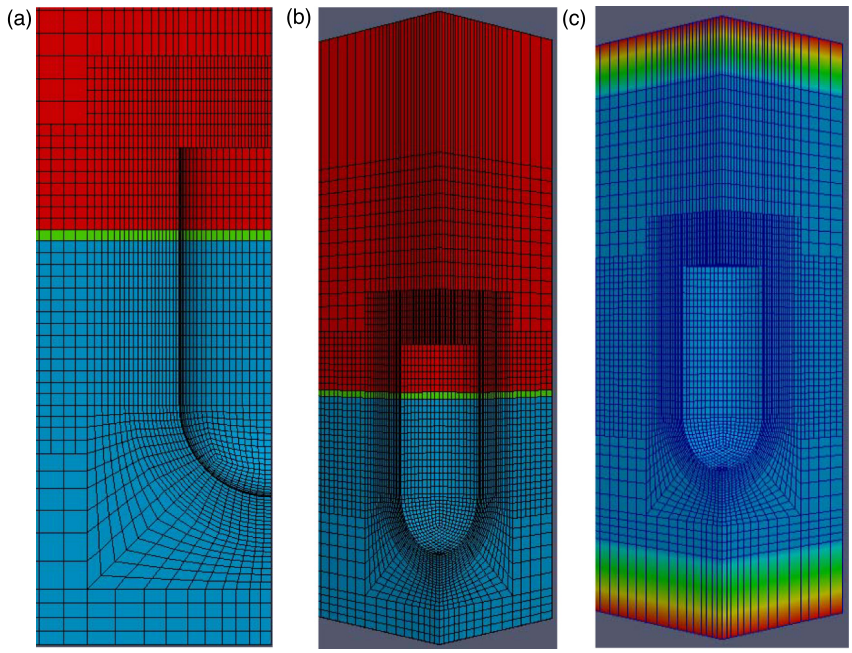

Fig. 8. (a) 2D view, initial condition (blue = water, red = air). (b) 3D cut out, initial condition (blue = water, red = air). (c) 3D view of the maximum displacement of the mesh points during the simulation, $t = 0.55$ s (blue = 0.231 m, red = 0 m). (For interpretation of the references to colour in this figure legend, the reader is referred to the web version of this article.)

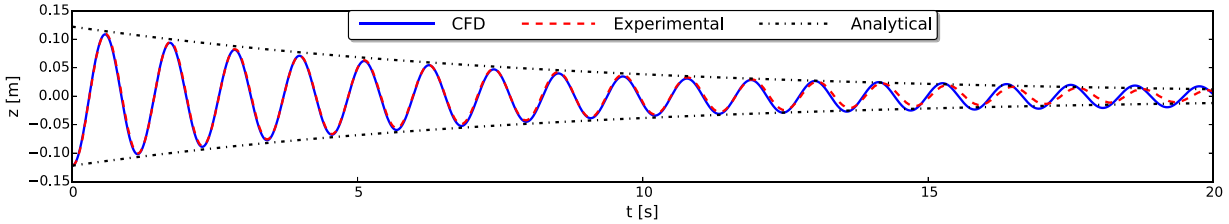

Fig. 9. Vertical position of the WEC during a free decay test with respect to its equilibrium position ($z^{eq} = 0$ m) obtained with CFD (continuous blue line) compared to the experimental decaying motion (dashed red line) and the analytical envelope (dashed–dotted black line). (For interpretation of the references to colour in this figure legend, the reader is referred to the web version of this article.)

4.1.3. Results

Firstly, Fig. 9 presents the vertical position of the WEC during a free decay test with an initial displacement $z^0 = -0.124$ m relative to its equilibrium position. The continuous blue line represents the numerical result while the dashed red line shows the experimental data. The dashed–dotted black line depicts the analytical envelope [20]. In general, Fig. 9 shows that the numerical result is in a very good agreement with the experimental decaying motion. After 13 s, some small discrepancies in the phase of the signal are observed between CFD and the experiment. This is caused by the different absorption methodology used in the numerical and experimental wave flume [20].

Secondly, the radiated wave field generated by the decaying motion of the WEC in calm water is captured by five wave gauges as indicated in the plan view of the wave flume in Fig. 10. The first gauge is installed closest to the absorbing boundary and its result is represented by the surface elevation η_1. The numerically obtained surface elevations are based on the volume fraction α in each computational cell. In a post processing step, the position of the free water surface is determined by a discrete integration of the volume fraction α over a vertical line (Z-direction) divided in n equal parts:

$$z_{water\ level} = \sum_{i=0}^{n-1} \alpha_i \left(z_{i+1} - z_i\right) \tag{39}$$

Fig. 11 shows the numerical and experimental results of the surface elevations. During the first 10 s, the amplitude as well as the phase of the radiated wave field is modelled very similar to the experimental data. Thereafter, some deviations between both results are observed. Again this observation is partially caused by the different absorption methodology used in the numerical and experimental wave flume [20].

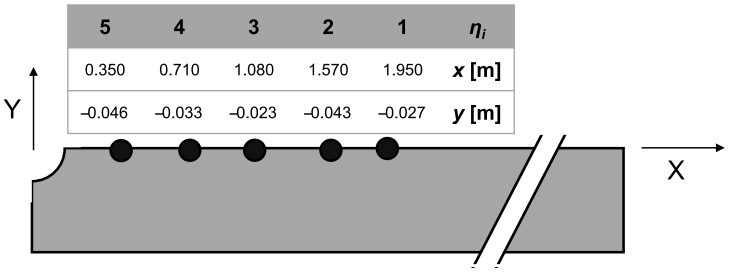

Fig. 10. Plan view of the five wave gauges inside the numerical wave flume. The WEC's centre ($x = 0$ m ; $y = 0$ m) is located at the upper left corner and the absorbing wave boundary condition is located at the right side of the domain ($x = 4.95$ m).

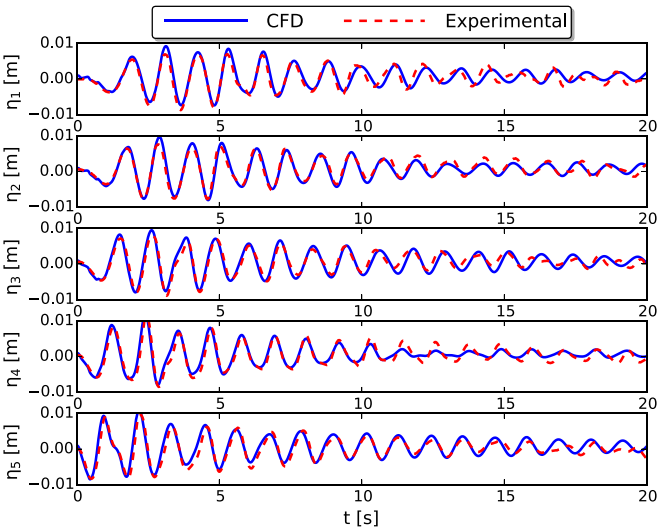

Fig. 11. The radiated wave field between the WEC including a linear damper and the wave paddle represented by the surface elevation η_i as a function of time t. (For interpretation of the references to colour in this figure legend, the reader is referred to the web version of this article.)

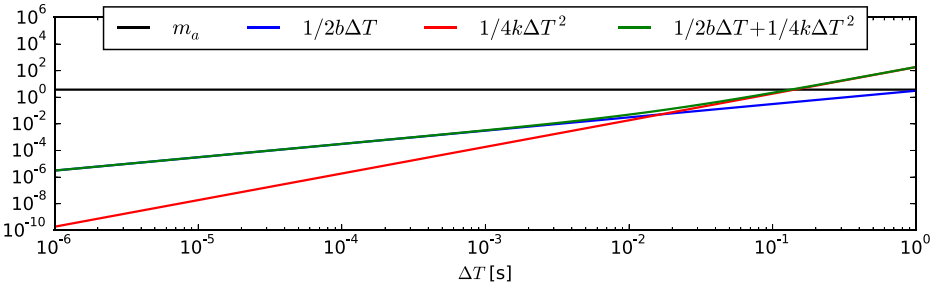

Fig. 12. Order of magnitudes of the terms in Eq. (32) as a function of ΔT for the free decay test of a WEC ($k = 745$ kg/s^2, $b = 6.19$ kg/s and $m_a = 3.74$ kg). (For interpretation of the references to colour in this figure legend, the reader is referred to the web version of this article.)

As mentioned in Section 3.2.1, the accelerated coupling algorithm assumes a dominant contribution of the added mass in Eq. (32). The methodology described in [20] gives values for $k = 745$ kg/s^2, $b = 6.19$ kg/s and $m_a = 3.74$ kg by using the time series of the WEC's decaying motion (Fig. 9). Fig. 12 shows the order of magnitude of each term in Eq. (32) as a function of ΔT on a log–log scale. It is demonstrated that the added mass (horizontal black line) is dominating for ΔT smaller than 0.13 s, which is always the case for this CFD simulation using a VoF method with a maximum Courant number of 0.3.

Fig. 13 depicts both the added mass coefficient m_a/m based on Eq. (34) and the relaxation factor α as a function of time. It is observed that the value of the added mass coefficient is always smaller than one. Strictly speaking, the accelerated coupling algorithm is not needed to stabilise the fluid–motion coupling for this test case. However, an efficient simulation is

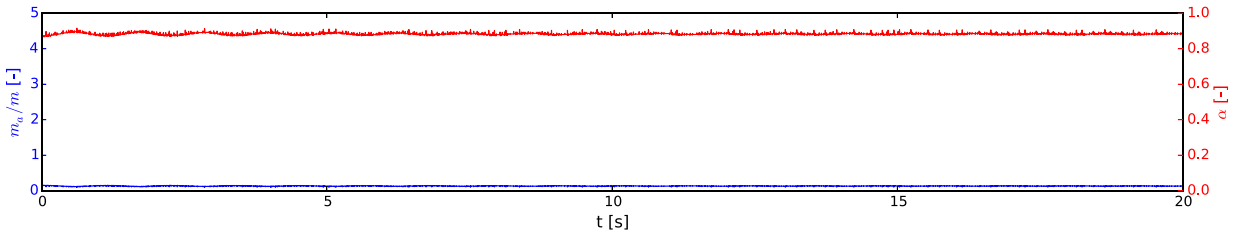

Fig. 13. Added mass coefficient m_a/m (in blue) and relaxation parameter α (in red) as a function of time during the free decay test of a WEC. (For interpretation of the references to colour in this figure legend, the reader is referred to the web version of this article.)

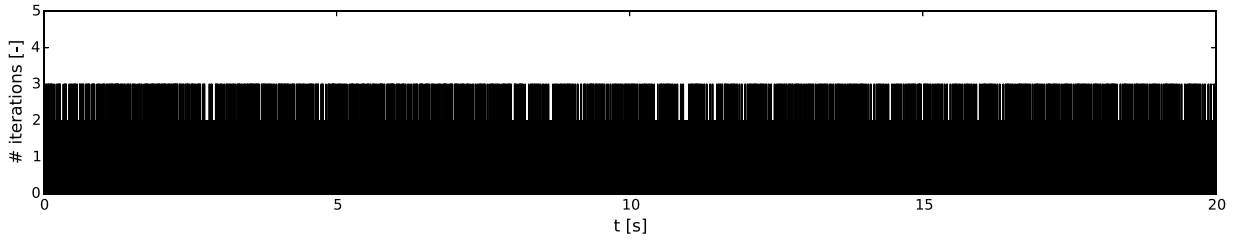

Fig. 14. The number of sub iterations for every time step during the free decay test of a WEC.

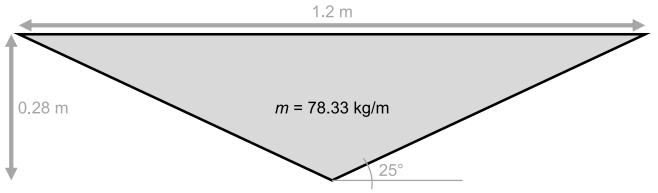

Fig. 15. Cross section of the wedge's geometry used during the experiments performed by [23].

still achieved since the number of sub iterations during every time step is mostly two or maximum three, as demonstrated in Fig. 14. This indicates the feasibility of the accelerated coupling algorithm for floating bodies with a small added mass effect.

4.2. Free falling wedge

The second and most challenging test case comprises a numerical verification and validation study of a free falling wedge with a significant added mass effect. Experimental data are available in Yettou et al. [23]. A definition sketch of the wedge's geometry is depicted in Fig. 15. The wedge, with a mass of 78.33 kg/m, is dropped 1.0 m above the water level. During the impact of the wedge with the water surface, turbulent effects are expected and a buoyancy-modified $k-\omega$ *SST* model is applied.

Giving the geometry of the experimental setup, numerical simulations are performed in 2D. As reported in e.g. [13], no additional features are expected in a 3D simulation. Note the difference with Section 4.1, where 3D simulations are required to obtain the hydrodynamic flow field in a good agreement with the experimental measurements.

4.2.1. Computational domain

Fig. 16 shows the computational domain of the 2DV simulation together with the boundary conditions types which are listed in the next paragraph 4.2.2. In order to speed up the simulations, a symmetry plane is used through the centre axis of the wedge simulating only half of the 30 m long domain. The total height of the domain is 3.59 m in the Z-direction and the water depth is equal to 1.0 m [23]. The initial state of the wedge is shown in Fig. 16 where the drop height above the water level is equal to 1.0 m.

After discretisation, the maximum size of a cell in both the horizontal X-direction Δx and vertical Z-direction Δz is equal to 0.04 m for the coarsest grid (grid 1, 18 000 cells). This results in an aspect ratio (i.e. the ratio of the cell size in horizontal to the vertical direction) equal to 1. The cells around the wedge are skewed as visualised in Fig. 17. Additionally, two more simulations are performed reducing Δx and the maximum of Δz to 0.02 m and 0.01 m, respectively, resulting in 72 000 cells (medium grid) and 285 000 cells (fine grid). A summary of the three meshes is provided in Table 2.

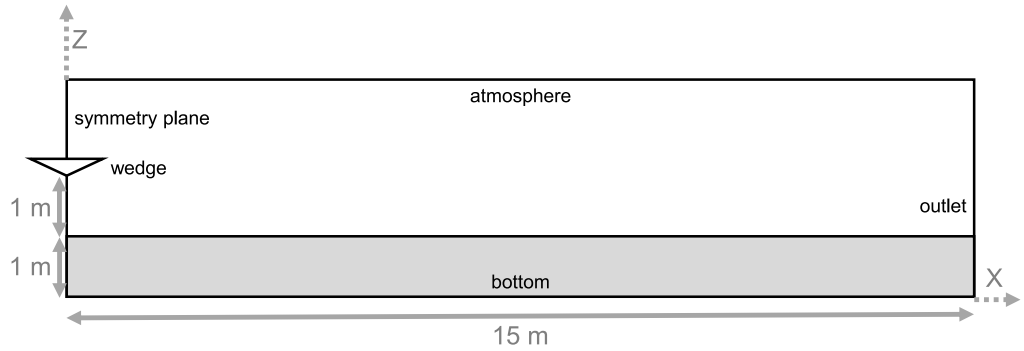

Fig. 16. A definition sketch showing the cross-section (*XZ*-direction) of the computational domain. The black words characterise the boundary condition type while the grey distances indicate the key sizes.

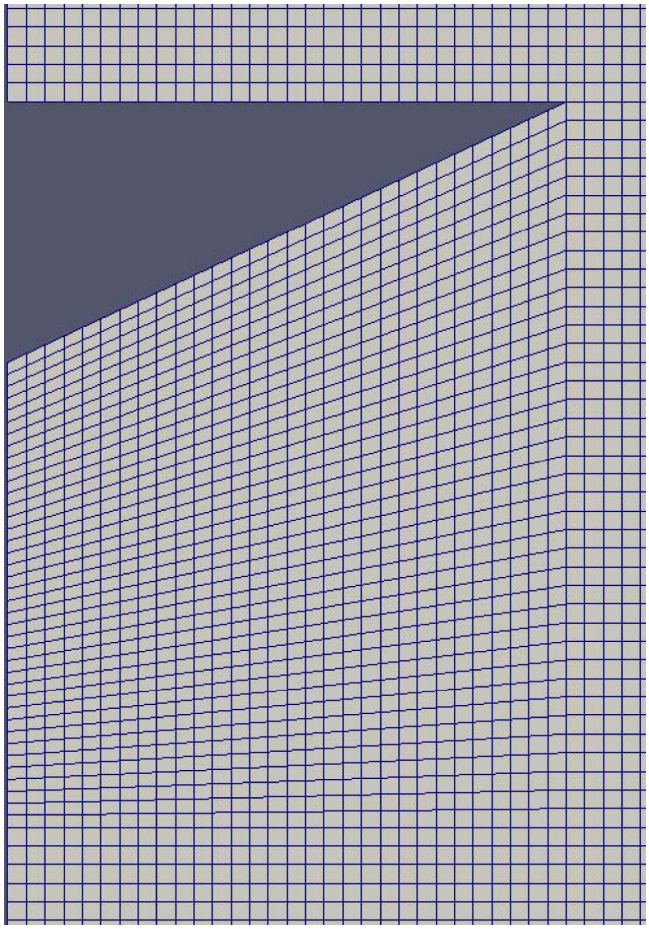

Fig. 17. A detail of the grid around the wedge.

Table 2
Mesh characteristics of the three different grids used.

Grid	Δx and max(Δz)	Cells
Coarse	0.04 m	18 000
Medium	0.02 m	72 000
Fine	0.01 m	285 000

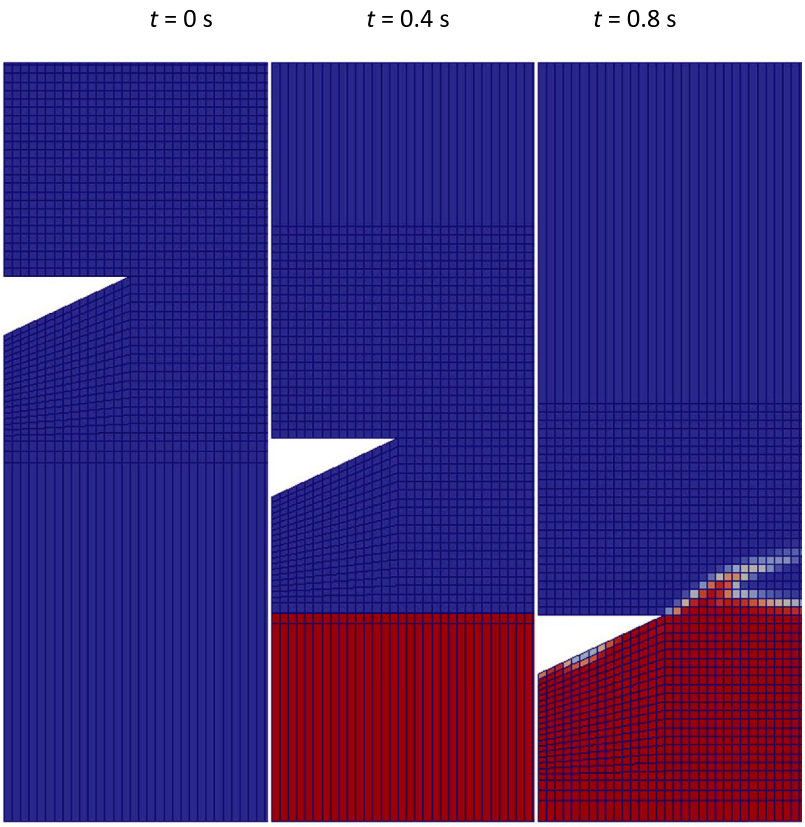

Fig. 18. Mesh motion for the free falling wedge simulation, air is shown in blue and water is shown in red. At $t = 0$ s, only air is present while for $t \geq 0.4$ s, also water is included in the computational domain. (For interpretation of the references to colour in this figure legend, the reader is referred to the web version of this article.)

4.2.2. Boundary conditions

The types of boundary conditions in a vertical plane are given in Fig. 16: symmetry plane on the left, outlet on the right, bottom, atmosphere and wedge. The bottom is modelled as a solid wall on which wall functions are activated for k and ω. A continuous wall function based on Spalding's law [24] switching between low- and high-Reynolds numbers is implemented for the turbulent viscosity ν_t. The initial values for k and ω in the computational domain are set to 10^{-10} m^2/s^2 and 1.0 s^{-1}, respectively. Furthermore on the bottom, a Dirichlet boundary condition is set for the velocity (0 m/s in the two directions) while the pressure and volume fraction are set to a Neumann condition. The outlet is implemented as a fully reflective wall by using identical boundary conditions as the bottom boundary. On all the boundary faces of the wedge, similar conditions are used as the bottom boundary except for the velocity vector which is set to a moving wall condition (see Eq. (15)). The atmospheric conditions at the top of the numerical domain are set to a mixed Dirichlet–Neumann boundary condition for the velocity, pressure and volume fraction. Finally, the value for δ in Eq. (35) is equal to 1.0 m/s^2.

4.2.3. Results

In this section, the numerical results of the free falling wedge are verified and validated by using experimental data obtained by [23]. Both, a mesh convergence study and temporal sensitivity study are performed followed by a discussion on the accelerated coupling algorithm. All the numerical simulations presented ran for 5 s. During the first 0.4 s, only air is present in the computational domain and consequently a single-phase flow simulation is performed. After 0.4 s, water is added to the domain and the two-phase flow simulation is started. This methodology is visualised in Fig. 18 and is needed to add the correct amount of water in the domain. Due to the large drop height, the cells in the lowest row have a height Δz equal to 1.7 m while the water depth during the experiment was only 1.0 m. Based on a preliminary simulation, Δz for the cells in the lowest row become smaller than 1.0 m for $t \geq 0.4$ s.

4.2.3.1. Mesh convergence study. For the mesh convergence study in this first subsection, three numerical simulations are presented using the grids mentioned in Table 2. A maximum Courant number of 0.3 is applied as discussed in Section 4.2.3.2. Figs. 19–21 depict, respectively, the vertical position, velocity and acceleration of the wedge as a function of time. The experimental data are shown using a dashed black line for the vertical position and velocity only. The numerical results

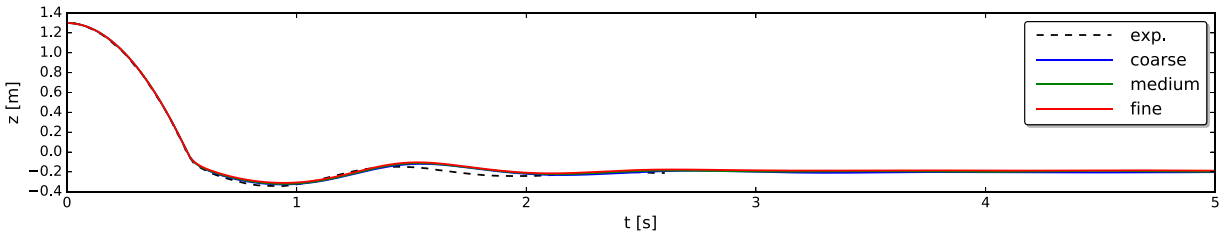

Fig. 19. Vertical position of the wedge as a function of time obtained numerically for three meshes (see Table 2) with a maximum Courant number of 0.3 (blue, green and red lines) and compared to experimental data [23] (dashed black line). (For interpretation of the references to colour in this figure legend, the reader is referred to the web version of this article.)

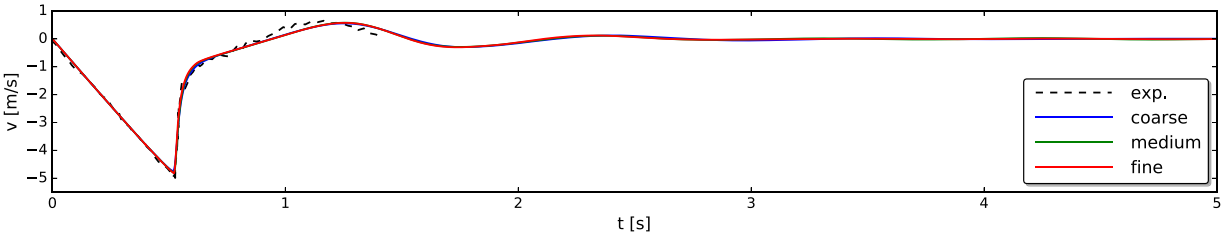

Fig. 20. Vertical velocity of the wedge as a function of time obtained numerically for three meshes (see Table 2) with a maximum Courant number of 0.3 (blue, green and red lines) and compared to experimental data [23] (dashed black line). (For interpretation of the references to colour in this figure legend, the reader is referred to the web version of this article.)

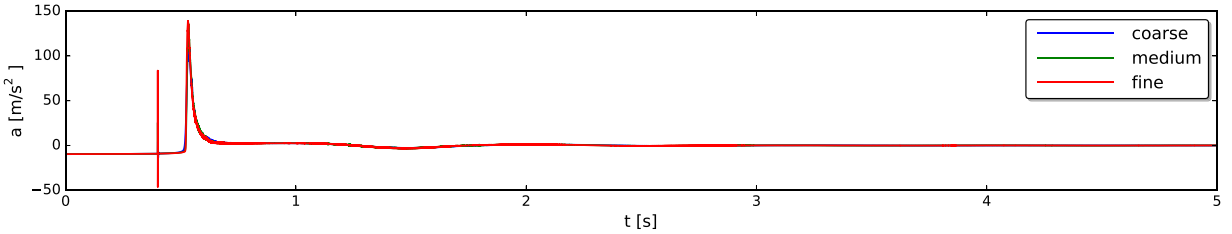

Fig. 21. Vertical acceleration of the wedge as a function of time obtained numerically for three meshes (see Table 2) with a maximum Courant number of 0.3 (blue, green and red lines). (For interpretation of the references to colour in this figure legend, the reader is referred to the web version of this article.)

are visualised by a blue, green and red line for the coarse, medium and fine grid, respectively. In general, only very small differences are visually observed between the three numerical simulations. The three numerical simulations are in a very good agreement with the experimental data for the vertical position and the velocity. For the vertical velocity, discrepancies between numerical and experimental results are visible between $t = 1.4$ s and $t = 2$ s. This is presumably caused by small friction forces due to the sliding mechanism in the experimental model which are neglected in the numerical setup. In Fig. 20, the abrupt change in velocity is due to the impact of the wedge on the water surface. It is observed that the impact is modelled in a very good agreement with the experimental measurements for the velocity of the wedge. Fig. 21 only presents numerical simulations for the vertical acceleration of the wedge as a function of time. At $t = 0.40$ s, a spike is observed in the wedge's acceleration. This is an artefact due to the addition of water in the computational domain as explained before and visualised in Fig. 18 but has no further impact on the results. In general, no significant differences are observed among the three numerical simulations, except for the peak values of the acceleration at the moment of impact (see detailed view in Fig. 22). The mesh convergence study is provided in Table 3 based on the peak value of the acceleration during the impact of the wedge on the water surface (see Fig. 22 around $t = 0.53$ s). The extrapolated values are computed with Richardson's extrapolation method: $a_{extra.} = a_{medium} + (a_{fine} - a_{medium})/(1 - 2^{-\alpha})$ with $\alpha = \ln((a_{coarse} - a_{medium})/(a_{medium} - a_{fine}))/\ln(2)$. $a_{extra.}$ can be regarded as the value calculated from the exact solution. As follows from Table 3, the solutions converge monotonically towards the exact solution and the medium grid returns an acceptable solution with an error of 3%.

4.2.3.2. Temporal sensitivity study. In this second subsection, three numerical simulations are presented using a maximum Courant number of 0.5, 0.3 and 0.1, respectively. Only the medium grid is considered since an error of 3% for the peak value of the acceleration during the water impact is found (see Table 2). Figs. 23–25 visualise again time series of, respectively, the vertical position, velocity and acceleration of the wedge. The experimental data are shown using a dashed black line while the numerical results are depicted in blue, green and red for a maximum Courant number of 0.5, 0.3 and 0.1, respectively. The

Table 3
Grid refinement study for the acceleration of the wedge. N_z is the number of cells in vertical direction. a is the maximum value of the acceleration during the water impact. $a_{\text{extra.}}$ is the exact solution.

Grid	N_z	a [m^2/s]	Error
Coarse	46	121.464	13.26%
Medium	94	135.814	3.01%
Fine	188	139.074	0.68%
$a_{extra.}$		140.032	

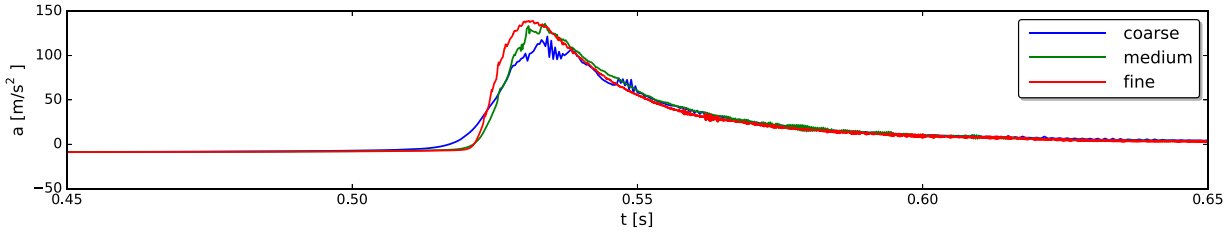

Fig. 22. Vertical acceleration of the wedge during the impact between $t = 0.45$ s and $t = 0.65$ s obtained numerically for three meshes (see Table 2) with a maximum Courant number of 0.3 (blue, green and red lines). (For interpretation of the references to colour in this figure legend, the reader is referred to the web version of this article.)

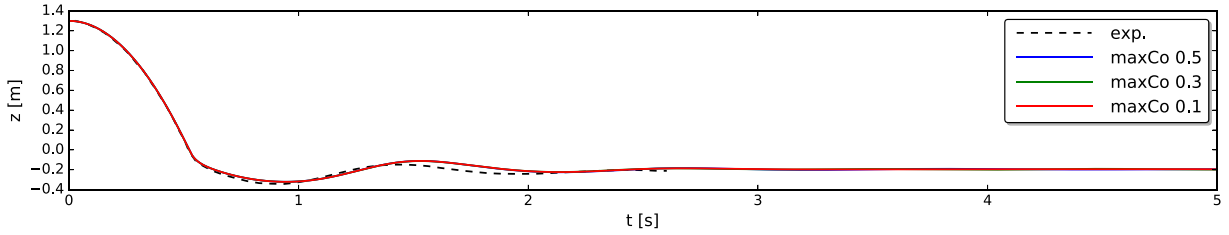

Fig. 23. Vertical position of the wedge as a function of time obtained numerically for the medium grid (see Table 2) with a maximum Courant number of 0.5, 0.3 and 0.1 (blue, green and red lines) and compared to experimental data [23] (dashed black line). (For interpretation of the references to colour in this figure legend, the reader is referred to the web version of this article.)

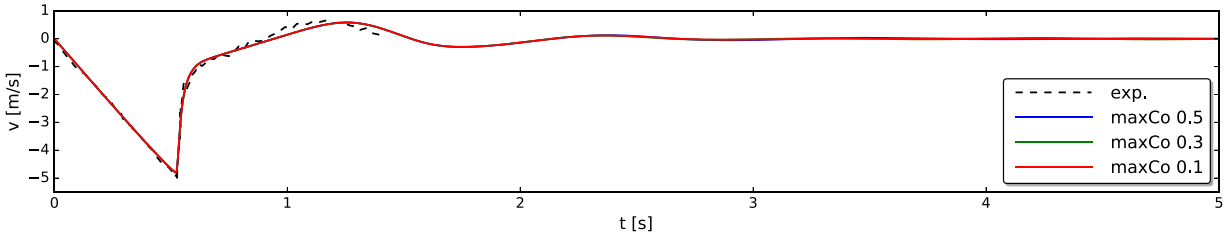

Fig. 24. Vertical velocity of the wedge as a function of time obtained numerically for the medium grid (see Table 2) with a maximum Courant number of 0.5, 0.3 and 0.1 (blue, green and red lines) and compared to experimental data [23] (dashed black line). (For interpretation of the references to colour in this figure legend, the reader is referred to the web version of this article.)

same observations are made as reported in Section 4.2.3.1: the three numerical simulations are very similar and are in a very good agreement with the experimental data for the vertical position and velocity of the wedge. Also for the acceleration, no differences are visually observed between the three numerical simulations provided in Fig. 25. Moreover as shown in Fig. 26, the peak value of the acceleration during the impact is not sensitive to the maximum Courant number. Based on our experience of using the VoF method for FSI simulations, we recommend a maximum Courant number of 0.3.

4.2.3.3. Acceleration of the coupling scheme. The achieved acceleration for the fluid–motion coupling is discussed using the medium grid with a maximum Courant number of 0.3. Firstly as mentioned in Section 3.2.1, the accelerated coupling algorithm requires a dominant contribution of the added mass in Eq. (32). Values for k, b and m_a are computed by using the time series of the wedge's motion. Only approximated values are calculated since they depend on the displaced volume of water which varies over time for the case of a wedge geometry:

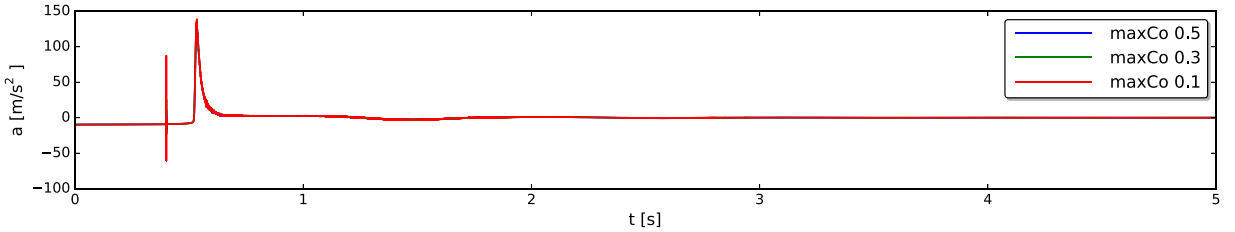

Fig. 25. Vertical acceleration of the wedge as a function of time obtained numerically for the medium grid (see Table 2) with a maximum Courant number of 0.5, 0.3 and 0.1 (blue, green and red lines). (For interpretation of the references to colour in this figure legend, the reader is referred to the web version of this article.)

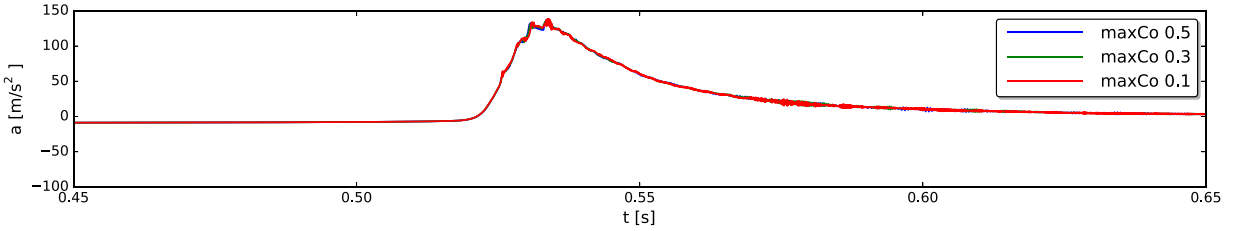

Fig. 26. Vertical acceleration of the wedge during the impact between $t = 0.45$ s and $t = 0.65$ s obtained numerically for the medium grid (see Table 2) with a maximum Courant number of 0.5, 0.3 and 0.1 (blue, green and red lines). (For interpretation of the references to colour in this figure legend, the reader is referred to the web version of this article.)

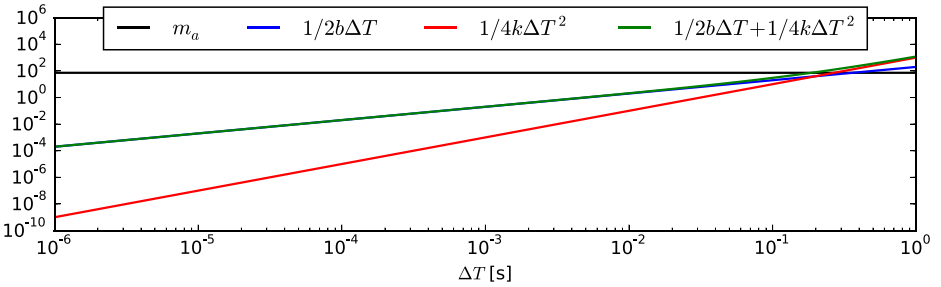

Fig. 27. Order of magnitudes of the terms in Eq. (32) as a function of ΔT for the 2D free falling wedge ($k = 4019$ kg/s^2/m, $b = 400$ kg/s/m and $m_a = 72$ kg/m). (For interpretation of the references to colour in this figure legend, the reader is referred to the web version of this article.)

- For k, the value at the moment of water entry is considered: $k = 4019$ kg/s^2/m;
- For b, the methodology described in [20] leads approximately to $b = 400$ kg/s/m;
- For m_a, a minimum value is the most severe condition and the methodology described in [20] gives approximately $m_a = 72$ kg/m.

Fig. 27 indicates that the added mass (black line) is dominating for ΔT smaller than 0.18 s, which is again always the case for this simulation.

Fig. 28 presents both the added mass coefficient m_a/m estimated by Eq. (34) and the relaxation factor α as a function of time. Fig. 29 depicts the number of sub iterations for every time step. Between 0 s and 0.5 s, the wedge is freely falling towards the water surface and is surrounded by air only. Due to the low density of air, the added mass is very small and only two sub iterations during every time step are needed to reach convergence between the fluid and motion solver. Around 0.5 s, the wedge is impacting on the water surface and the added mass coefficient increases up to four times the mass of the wedge. As a result of our accelerated coupling algorithm, the relaxation factor lowers to reduce the number of sub iterations. Based on Fig. 29, only a large number of sub iterations is simulated at the moment when the wedge is touching the water surface. Thereafter, the motion of the wedge is decaying and the added mass is changing over time and therefore only two, occasionally three, sub iterations are needed to obtain convergence between the fluid and motion solver.

5. Conclusions

In this paper, we presented an accelerated coupling algorithm between a two-phase fluid solver and a motion solver to perform FSI simulations of a floating body. The coupling algorithm is applying multiple sub iterations during every time step

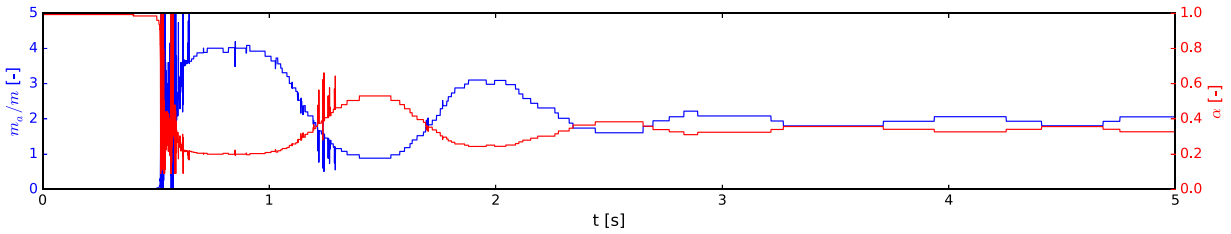

Fig. 28. Added mass coefficient m_a/m (in blue) and relaxation parameter α (in red) as a function of time using the medium grid (see Table 2) with a maximum Courant number of 0.3. (For interpretation of the references to colour in this figure legend, the reader is referred to the web version of this article.)

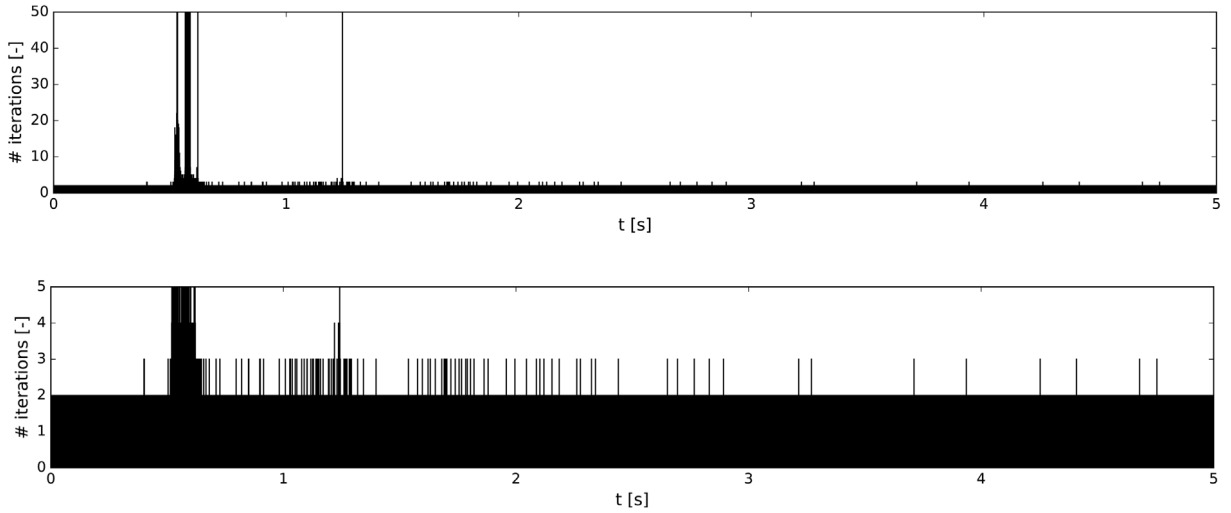

Fig. 29. The number of sub iterations for every time step using the medium grid (see Table 2) with a maximum Courant number of 0.3. Top graph: maximum 50 sub iterations on the vertical axis. Bottom graph: detail of the top graph where only 5 sub iterations are shown on the vertical axis.

in the transient simulation to reach convergence between the fluid and motion solver. The convergence speed is enhanced by using our accelerated coupling algorithm by calculating a Jacobian, based on the available solutions of previous sub iterations for the acceleration of the floating body and the force acting on it. This method results in efficient simulations for body geometries with a significant added mass effect. The coupled fluid–motion solver is applied to two different floating bodies: a free decay test of a WEC (small added mass effect) and a free falling wedge impacting the water surface (significant added mass effect). For both test cases, numerical results are validated by using experimental data. Firstly, the WEC's heave motion and radiated wave field during the free decay test are very similar to the experimental measurements. Secondly for the free falling wedge, a good agreement between numerical and experimental data is found for the wedge's vertical position and velocity. We demonstrated the successful capability of the coupled fluid–motion solver using an accelerated coupling algorithm in order to efficiently simulate heaving floating bodies with a significant reduced computational cost.

Acknowledgement

The first author is Ph.D. fellow of the Research Foundation – Flanders (FWO), Belgium (Ph.D. fellowship 1133817N).

References

[1] J. Davidson, S. Giorgi, J.V. Ringwood, Linear parametric hydrodynamic models for ocean wave energy converters identified from numerical wave tank experiments, Ocean Eng. 103 (2015) 31–39, http://dx.doi.org/10.1016/j.oceaneng.2015.04.056.

[2] H.A. Wolgamot, C.J. Fitzgerald, Nonlinear hydrodynamic and real fluid effects on wave energy converters, Proc. Inst. Mech. Eng. A 229 (2015) 772–794, http://dx.doi.org/10.1177/0957650915570351.

[3] E.J. Ransley, D. Greaves, A. Raby, D. Simmonds, M. Hann, Survivability of wave energy converters using CFD, Renew. Energy 109 (2017) 235–247, http://dx.doi.org/10.1016/j.renene.2017.03.003.

[4] J. Davidson, C. Windt, G. Giorgi, R. Genest, J.V. Ringwood, Evaluation of energy maximising control systems for wave energy converters using openFOAM for wave energy converters using openFOAM, in: M. Nobrega, H. Jasak (Eds.), OpenFOAM - Sel. Pap. from 11th Work, Springer International Publishing, 2018.

[5] J. Degroote, Partitioned simulation of fluid-structure interaction, Arch. Comput. Methods Eng. 20 (2013) 185–238, http://dx.doi.org/10.1007/s11831-013-9085-5.
[6] H. Söding, How to integrate free motions of solids in fluids, in: 4th Numer. Towing Tank Symp. Hambg., 2001.
[7] A. Babarit, G. Delhommeau, Theoretical and numerical aspects of the open source BEM solver NEMOH, in: Proc. 11th Eur. Wave Tidal Energy Conf., 2015.
[8] A. Leroyer, M. Visonneau, Numerical methods for RANSE simulations of a self-propelled fish-like body, J. Fluids Struct. 20 (2005) 975–991, http://dx.doi.org/10.1016/j.jfluidstructs.2005.05.007.
[9] J. Vierendeels, K. Dumont, E. Dick, P. Verdonck, Analysis and stabilization of fluid-structure interaction algorithm for rigid-body motion, AIAA J. 43 (2005) 2549–2557.
[10] U. Küttler, W.A. Wall, Fixed-point fluid–structure interaction solvers with dynamic relaxation, Comput. Mech. 43 (2008) 61–72, http://dx.doi.org/10.1007/s00466-008-0255-5.
[11] A.J. Dunbar, B.A. Craven, E.G. Paterson, Development and validation of a tightly coupled CFD/6-DOF solver for simulating floating offshore wind turbine platforms, Ocean Eng. 110 (2015) 98–105, http://dx.doi.org/10.1016/j.oceaneng.2015.08.066.
[12] J.H. Chow, E.Y.K. Ng, Strongly coupled partitioned six degree-of-freedom rigid body motion solver with Aitken's dynamic under-relaxation, Int. J. Nav. Archit. Ocean Eng. 8 (2016) 320–329, http://dx.doi.org/10.1016/j.ijnaoe.2016.04.001.
[13] A. Kamath, H. Bihs, Ø.A. Arntsen, Study of water impact and entry of a free falling wedge using computational fluid dynamics simulations, J. Offshore Mech. Arctic Eng. 139 (2017) 31802, http://dx.doi.org/10.1115/1.4035384.
[14] I. Gatin, V. Vukčević, H. Jasak, H. Rusche, Enhanced coupling of solid body motion and fluid flow in finite volume framework, Ocean Eng. 143 (2017) 295–304, http://dx.doi.org/10.1016/j.oceaneng.2017.08.009.
[15] OpenFOAM®, OpenFOAM-3.0.1, 2015.
[16] E. Berberović, N.P. van Hinsberg, S. Jakirlić, I.V. Roisman, C. Tropea, Drop impact onto a liquid layer of finite thickness: Dynamics of the cavity evolution, Phys. Rev. E. 79 (2009) 36306, http://dx.doi.org/10.1103/PhysRevE.79.036306.
[17] B. Devolder, P. Rauwoens, P. Troch, Application of a buoyancy-modified k-ω SST turbulence model to simulate wave run-up around a monopile subjected to regular waves using OpenFOAM®, Coastal Eng. 125 (2017) 81–94, http://dx.doi.org/10.1016/j.coastaleng.2017.04.004.
[18] B. Devolder, P. Troch, P. Rauwoens, Performance of a buoyancy-modified k-ω and k-ω SST turbulence model for simulating wave breaking under regular waves using OpenFOAM®, Coastal Eng. 138 (2018) 49–65, https://doi.org/10.1016/j.coastaleng.2018.04.011.
[19] F.R. Menter, J.C. Ferreira, T. Esch, The SST turbulence model with improved wall treatment for heat transfer predictions in gas turbines, Int. Gas Turbine Congr. 2003 (2003) 1–7.
[20] B. Devolder, P. Rauwoens, P. Troch, Numerical simulation of a single Floating Point Absorber Wave Energy Converter using OpenFOAM®, in: Prog. Renew. Energies Offshore, CRC Press, 2016, pp. 197–205, http://dx.doi.org/10.1201/9781315229256-25.
[21] P. Higuera, J.L. Lara, I.J. Losada, Realistic wave generation and active wave absorption for Navier–Stokes models. Application to OpenFOAM., Coastal Eng. 71 (2013) 102–118, http://dx.doi.org/10.1016/j.coastaleng.2012.07.002.
[22] P. Higuera, J.L. Lara, I.J. Losada, Simulating coastal engineering processes with OpenFOAM., Coastal Eng. 71 (2013) 119–134, http://dx.doi.org/10.1016/j.coastaleng.2012.06.002.
[23] E.-M. Yettou, A. Desrochers, Y. Champoux, Experimental study on the water impact of a symmetrical wedge, Fluid Dyn. Res. 38 (2006) 47–66, http://dx.doi.org/10.1016/j.fluiddyn.2005.09.003.
[24] D.B. Spalding, A single formula for the Law of the Wall, J. Appl. Mech. 28 (1961) 455, http://dx.doi.org/10.1115/1.3641728.